LAWRENCE
LIVERMORE
NATIONAL
LABORATORY

LLNL-JRNL-858747

The Intrinsic Mechanical Properties of Hydromagnesite, $Mg_5(CO_3)_4(OH)_2 \cdot 4H_2O$, a Key Phase of Reacticve MgO Cement

J. Li, W. Zhang

January 3, 2024

Cement and Concrete Research

Disclaimer

The Intrinsic Mechanical Properties of Hydromagnesite, $Mg_5(CO_3)_4(OH)_2 \cdot 4H_2O$, a Key Phase of Reactive MgO Cement

Wenxin Zhang[1,2], Jiaqi Li[1]*

Affliations:
[1]Atmospheric, Earth, and Energy Division, Lawrence Livermore National Laboratory, 7000 East Avenue, Livermore, CA 94550, United States
[2]Division of Engineering and Applied Sciences, California Institute of Technology, 1200 E. California Blvd., Pasadena, CA 91125, United States
*Corresponding author. Email: li88@llnl.gov

Abstract
To potentially enable CO_2 sequestration, reactive MgO cement is emerging as an alternative binder to Portland cement. Understanding the mehcanical properties of its binding phase is critical for understanding the strength development and performing materials design for reactive MgO cement systems; however, the intrinsic mechanical properties of hydromagnesite ($Mg_5(CO_3)_4(OH)_2 \cdot 4H_2O$), a key binding phase, remains unexplored. The present study utilized synchrotron-based high-pressure X-ray diffraction to determine the unit cell-scale, intrinsic mechanical properties of hydromagnesite for the first time. Up to hydrostatic loading of 7.7 GPa, the bulk modulus of hydromagnesite was determined as 59 GPa or 71 GPa fitted using second-order or third-order Birch-Murnaghan equation of state, which we contextualize with binding phases in various cement systems. The experiment results are applicable in materials design of low-carbon concrete and valuable for the validation and calibration of atomistic models.

Keywords: reactive MgO cement; carbonation; alternative cement; CO_2 sequestration

1. Introduction
Portland cement production contributes to ~7% of annual global anthoprogenic greenhouse gas emissions [1]. Cement decarbonation at scale is of great interest to the industry, with substantial efforts having been made to decarbonize cement and concrete for various applications [2]. Among many emerging decarbonization technologies in the industry, alternative binders that directly react with and sequester CO_2 have recently been investigated extenstively due to the global emphasis on climate change mitigation and on carbon capture, utilization, and storage (CCUS) [3]. These alternative binders harden via the mineralization process between CO_2 and Mg^{2+}/Ca^{2+} from hydroxides, oxides, or silicates, upraising Calera, Fortera, and Solidia as successful industrial pioneers [4]–[6].

Reactive MgO cement, produced from calcining magnesite ($MgCO_3$) or brucite ($Mg(OH)_2$), is a promising low-carbon alternative binder when Mg is extracted from low-carbon sources (e.g., magnesium silicate rocks) [3]. Reactive MgO cement can bind CO_2 to form hydrated magensium carboantes [7]. The reactive MgO is typically light-burnt at temperatures as low as 700°C and endowed with a porous microstructure and large specific surface area leading towards high reactivity with CO_2. The reactive MgO cement shows comparable compressive strength to ordinary Portland cement while possessing lower embodied carbon [8], [9]. The mechanical properties of reactive MgO cement depend on many factors, e.g., degree of carbonation, pore structure, and binding phases [10]. Multiple hydrated magnesium carbonate phases may form during carbonation: nesquehonite ($MgCO_3 \cdot 3H_2O$), dypingite ($Mg_5(CO_3)_4(OH)_2 \cdot 5H_2O$), hydromagnesite ($Mg_5(CO_3)_4(OH)_2 \cdot 4H_2O$), and artinite ($Mg_2(CO_3)(OH)_2 \cdot 3H_2O$) – their preferential formations are governed by temperature, relative humidity, pH, and CO_2 abundance [11]. The binding phases affect strengths through two primary mechanisms: (i) the different crystallite geometries guide different microstructure formation of hardened pastes, resulting in different porosity and pore connectivity; and (ii) the unit cell-level intrinsic mechanical properties, e.g., bulk modulus, specific to each crystalline phase distinguish the cement paste-level mechanical properties based on the phase present [12].

Understanding the intrinsic mechanical properties of hydrated magnesium carbonates is fundamental to optimizing the mechanical properties of reactive MgO cement, especially in the framework of bottom-up materials design. This information is essential to experimental validations to computational modeling, e.g. molecular dynamics simulations, yet it is inaccessible by most experimental techniques, e.g.,

nanoindenation, which is only capable of probing the micromechanical properties of hardened cement systems. High-pressure X-ray diffraction (HP-XRD) serves as a powerful technique that probes the crystal lattice properties of individual phases [13], eliminating the influences of hardened paste-level microstructure, e.g., presence of pores and preferred orientation, which other characterization techniques like nanoindentation are inevitably affected by [13], [14].

Hydromagnesite is the most common hydrated magnesium carbonate in nature and in concrete (as a phase in hydrated pastes and cold-fusion aggregates). It belongs to the monoclinic $P2_1/c$ space group (Fig. 1) [15]. The present HP-XRD study evaluates the previously unexplored intrinsic mechanical properties of hydromagnesite.The results are discussed in comparison with common binding phases in other cement systems. The work provides important implications to the validation of force fields used in molecular dynamic simluations and approximation methods in density functional theory calculations.

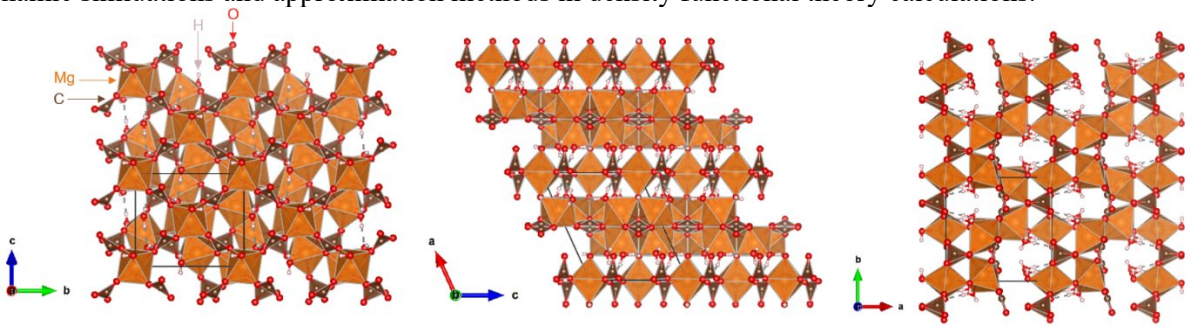

Figure 1. Crystal structure of hydromagnesite viewed along different axis. Mg–O octahedra are shown in orange, C–O planar triangle in brown, oxygen atoms in red, and hydrogen atoms in grey. The unit cell is indicated by the black box. Hydrogen bonds are indicated by the dashed lines.

2. Methods

The as-received hydromagnesite sample ($Mg_5(CO_3)_4(OH)_2 \cdot 4H_2O$; Fisher; 99% purity) was dry-ground using a mortar followed by sieving using a 10 μm screen, with estimated particle size of <10 μm, before the high-pressure X-ray diffraction (HP-XRD) experiemnt at beamline 12.2.2 of the Advanced Light Source at the Lawrence Berkeley National Laboratory. The measurements were performed using a monochromatic synchrotron X-ray with the sample in a Merrill-Bassett diamond anvil cell by the transmission-mode Laue method. Before mounting the powdery hydromagnesite sample, we first used the diamond anvil pair (D_{culet} = 300 μm) to pre-indent the stainless-steel gasket until an indent depth of 80 μm and used laser milling to drill a cylindrical chamber (D = 100 μm) at the center of the indent. Next, the sample and then a small spherical ruby (α-Al_2O_3 doped with 0.05 wt.% Cr^{3+}) were loaded into the chamber. Lastly, we filled the chamber with a pressure-transmitting medium (methanol-to-ethanol volumeric ratio = 4:1) and sealed the chamber with the diamond anvil pair.

The wavelength of the incident X-ray beam was 0.4940 Å, the sample-to-detecter distance was 330 mm, and the slit-shaped beam cross-section was ~30-μm wide. The diamond anvil cell setup was used throughout the experiment, where the hydrostatic pressure, P, was determined during X-ray measurement intervals using the ruby fluorescence technique [32], except that for ambient-pressure reference measurement, the ground hydromagnesite was directly loaded to a glass capillary instead of the anvil cell. Dioptas [16] was used for calibration and for converting the raw 2D-image data into the line profile; XFIT code [17] was used for deconvoluting diffraction peaks and extracting their positions (peak type = split Pearson VII; fitting method = Marquardt); Celref [18] was used for refining the lattice parameters – unit cell edge lengths a, b, c and angle β (fixing the other two angles α = γ = 90°) at each applied hydrostatic pressure. Subsequently, the unit cell volume, V, was calculated at each pressure as

$$V = abc(1 - cos^2\alpha - cos^2\beta - cos^2\gamma + 2cos\alpha \cdot cos\beta \cdot cos\gamma)^{1/2} \qquad \text{(eq.1)}$$

and the bulk modulus, K_0, was estimtaed by the least-square regression using the second-order Birch-Murnaghan equation of state (BM-EoS), where V_0 represents V under the ambient condition:

$$P = \frac{3}{2}K_0\left[\left(\frac{V}{V_0}\right)^{-\frac{7}{3}} - \left(\frac{V}{V_0}\right)^{-\frac{5}{3}}\right] \qquad \text{(eq.2)}$$

Which has been widely applied for various cement-related phases for measurements at relatively low pressures of below 10 GPa, which typically corresponding to $V/V_0 \gtrsim 0.9$ [19, 25], as a simplification from the third-order BM-EoS by taking $K_0' = 4$:

$$P = \frac{3}{2}K_0\left[\left(\frac{V}{V_0}\right)^{-\frac{7}{3}} - \left(\frac{V}{V_0}\right)^{-\frac{5}{3}}\right]\left[1 + \frac{3}{4}(K_0' - 4)\left(\left(\frac{V}{V_0}\right)^{-\frac{2}{3}} - 1\right)\right] \qquad \text{(eq.3)}$$

3. Results and Discussion

Fig. 2A presents the diffractograms of hydromagnesite – from bottom to top, the ambient and loading/unloading-cycle measurements. The two diffraction peaks at ~ 0.12 and 0.49 $Å^{-1}$ not present in the ambient reference are attributed to diffraction from the steel gasket, as the vertical dimension of the beam cross-section could exceed the range of the sample chamber, while no additional impurities were observed. From the raw 2D pattern (insets to Fig. 2A), the uniform intensity of all diffraction rings irrespective of the azimuthal angle or the loading pressure confirms the absence of any preferred orientation, which in turn indicates deviatoric stress-free, purely hydrostatic stress states as it has been shown in HP-XRD studies of other anisotropic cement-related crystalline phases that applying deviatoric stress induces preferred re-orientation of the most compliant crystallographic orientation to the loading axis [14]. Systematic position shifts of diffraction peaks were observed alongside the hydrostatic pressurization, where a shift to higher d^{-1} suggests decreased lattice interplanar spacings due to compressive loading. At higher elevated pressures, the diffraction peaks generally became less intense and more diffuse, suggesting possible increased microstrains and structural disorder, which are regularly identified in high-pressure studies [20]. Figs. 2B and 2C examines the diffraction peak broadening, via the full width at half maximum (FWHM). In the context of Williamson-Hall uniform stress deformation model, the broadening comprises of a constant component inversely proportional to the crystallite size and a varying component linear to d^{-1} at a slope of σ/E_{hkl}, microstress normalized to the Young's modulus specific to the (*hkl*) plane [30,31]. Fig. 2B demonstrates the systematic increase in FWHM with increasing hydrostatic pressure for selected (*hkl*) diffraction peaks. The lines are not straight for each loading step due to anistropic E_{hkl}, a lack of information of which precludes more quantitative fitting. Fig. 2C further demonstrates the significant linear correlation between FWHM and hydrostatic pressure, suggesting microstrain as the primary origin of broadening, while the (hkl)-specific slopes are ascribed to their different $(d_{hkl})^{-1}$ and different E_{hkl}. Besides, no obvious coalesce of pre-existing diffraction peaks or emergence of new diffraction peaks were observed, suggesting that hydromagnesite did not go through phase transformation or amorphization up to 7.7 GPa. The fully unloaded diffractogram highly matches the ambient reference in their diffraction peak positions and relative intensities, indicating minimal residual lattice strain.

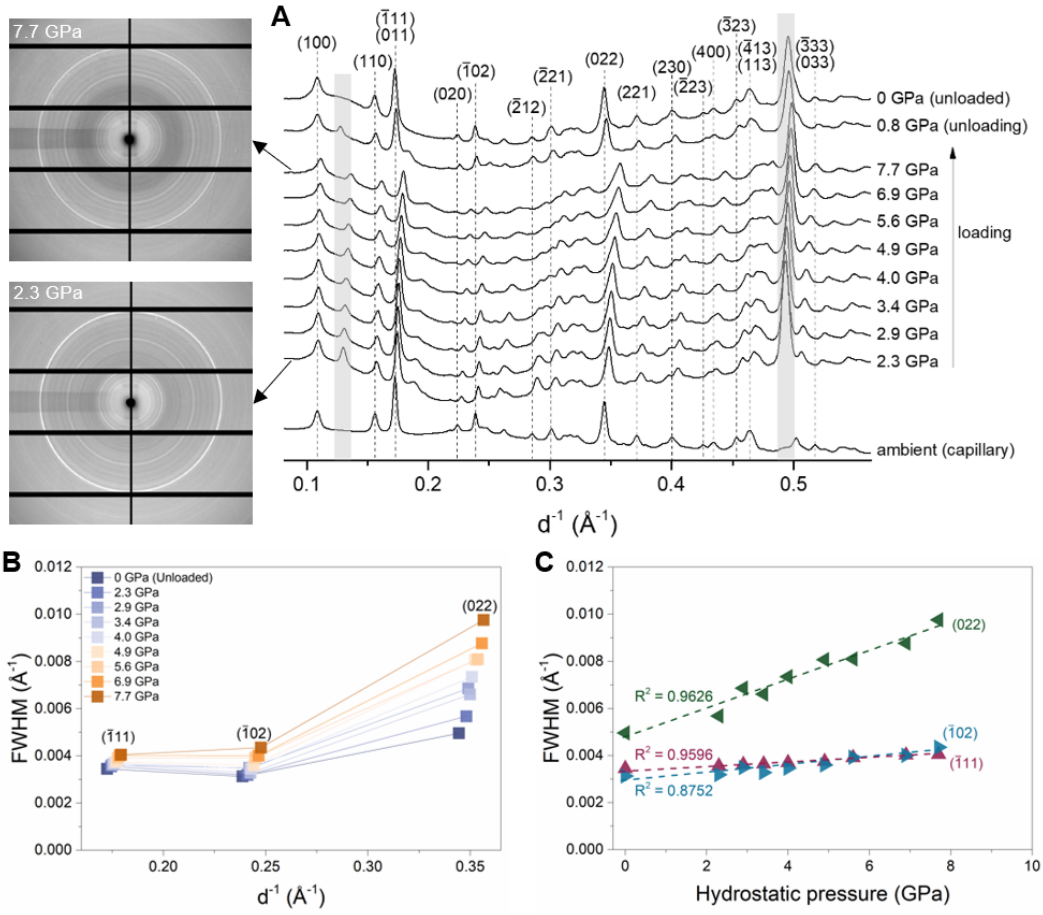

Figure 2. (**A**) The diffractograms of hydromagnesite under different hydrostatic pressure, insets showing raw 2D diffraction pattern measurements at the first and maximum loading steps. Dashed lines are aligned with the diffraction peak positions in the ambient (capillary) reference measurement for eye guidance. (**B** and **C**) Broadening of diffraction peaks as a function of d^{-1} and hydrostatic pressure, respectively.

Table 1. Unit cell parameters for hydromagnesite as a function of applied hydrostatic pressure. Pressure errors are < 0.15 GPa. The errors of lattice parameters are <0.05%.

	***P* (GPa)**	***a* (Å)**	***b* (Å)**	***c* (Å)**	**β (°)**	***V* (Å^3)**
Ambient	0	10.103	8.924	8.378	114.29	688.4
Loading	2.3	10.043	8.792	8.293	114.27	667.5
	2.9	10.017	8.760	8.267	114.09	662.3
	3.4	10.002	8.726	8.249	114.15	657.0
	4.0	9.980	8.698	8.228	114.09	652.0
	4.9	9.962	8.646	8.189	114.13	643.7
	5.6	9.957	8.609	8.162	114.24	637.9
	6.9	9.902	8.553	8.117	114.11	627.4
	7.7	9.859	8.528	8.082	114.05	620.5
Unloading	0.8	10.086	8.847	8.343	114.3	678.5
Unloaded	0	10.111	8.922	8.376	114.29	688.7

The evolution of the refined unit-cell parameters of hydromagnesite as a function of *P* is summarized in Table 1, showing monotonic decrease in *a*, *b*, and *c* and fluctuation in β during loading. The **a**, **b**, and **c**-axial Biot strain, $\varepsilon_a = (a - a_0)/a_0$, $\varepsilon_b = (b - b_0)/b_0$, and $\varepsilon_c = (c - c_0)/c_0$, are therefore calculated with respect to the reference measurement and plotted as a function of *P* (Fig. 3A). Least-square linear fitting is applied to extract the axial incompressibility, up to 7.7 GPa. The material is highly anisotropic along the three unit-cell axial directions. The highest axial incompressibility of –1/335 GPa^{-1} for the **a**-axis is attributed to the continuous chain of Mg–O octahedra along **a**-axis, where every three units form one edge-sharing and two

corner-sharing; the intermediate axial incompressibility of –1/219 GPa^{-1} for the **c**-axis is attributed to the edge-sharing Mg–O octahedra pairs jointed with C–O planar triangles by corner sharing along the **c**-axis; the lowest axial incompressibility of –1/171 GPa^{-1} for the **b**-axis is explained by the lack of (i) the chain of Mg–O octahedra and (ii) H-bonding network, which are present only in the orthogonal **a**-**c** plane. After unloading, the axial strains were all fully recovered. The value of β, the monoclinic angle between **a**- and **c**-axis, fluctuated close to the ambient value (by < 0.3° or 0.2%) up to the highest 7.7-GPa loading step and fully recovered after reloading to the ambient condition (Fig. 3B).

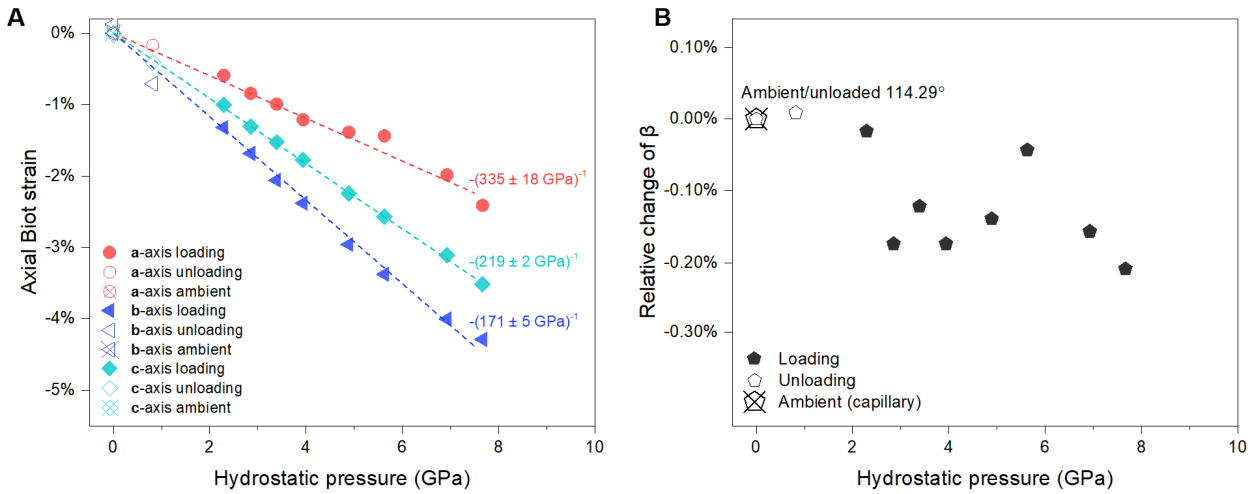

Figure 3. (**A**) Axial Biot strain along **a**-, **b**-, and **c**-axis; (**B**) relative change of monoclinic angle β as a function of hydrostatic pressure.

Table 2. Birch-Murnaghan Equation of State fitting for hydromagnesite.

	K_0 (GPa)	K_0'	V_0 (Å^3)
2nd order	58.7 ± 1.6	4 (fixed)	691.4 ± 1.2
3rd order	71.2 ± 1.6	1.13 ± 0.31	688.6 ± 0.4

The volumetric strain, calculated based on the reference measurement, is plotted against *P* in Fig. 4A, along with the BM-EoS fitting curves. The fitted parameters to both 2nd and 3rd order BM-EoS are summarized in Table 2. From the least-square regression fitting, we determined the bulk modulus of hydromagnesite to be 58.7 GPa by the 2nd-order BM-EoS (71.2 GPa by the 3rd-order BM-EoS), with < 3% standard error. Note that the unloading point (*P* = 0.8 GPa) is not considered in axial incompressibility or bulk modulus estimations; its slight deviation from the general trendline possibly resulted from inaccurate pressure measurement during partial unloading as the dynamic unloading recovery process takes time.

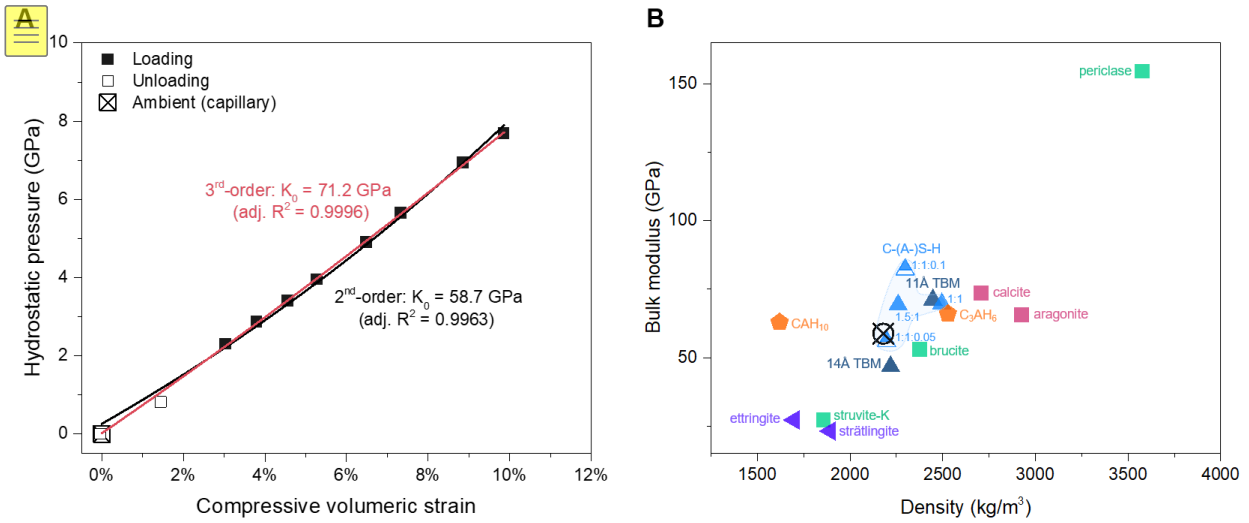

Figure 4. Bulk modulus. (A) Hydrostatic pressure as a function of compressive volumetric strain for hydromagnesite. The black and the red solid lines represent the regression curve to the 2nd- and 3rd-order BM-EoS, respectively. The error in volumetric strain is typically < 1%. **(B) Bulk modulus of phases related to cement systems as a function of material density.** The present result of hydromagnesite is represented by the black marker. Portland cement-related phases are represented by blue triangles, calcium-aluminate cement-related phases in orange, green squares for magnesium phosphate cement-related phases, pink squares for calcium carbonates, and purple triangles for phases present in multiple cement systems. C-(A-)S-H stands for calcium (alumino)silicate hydrates, labeled with the respective Ca/Si (or Ca/Si/Al) atomic ratio. CAH_{10} stands for $CaO{\cdot}Al_2O_3{\cdot}10H_2O$, and C_3AH_6 for $3CaO{\cdot}Al_2O_3{\cdot}6H_2O$. All bulk modulus values are obtained with the second-order BM-EoS as did in the original literature [13], [20-22], [24-26] or fitted using the original data [23], [27].

The bulk modulus-density relation of hydromagnesite as a key binding phase in reactive MgO cement, a carbonation-based cement, is compared with various binding phases from a range of cement systems. Fig. 4B presents the general positive correlation between density and bulk modulus. Specifically, hydromagnesite falls comparable to the synthetic calcium (alumino)silicate hydrates (C-(A-)S-Hs [21]), the primary binding phase in Portland cement systems, at various compositions and to tobermorites [20], the crystalline model mineral for C-(A-)S-Hs, in terms of both bulk modulus and density. These C-(A-)S-H phases comprise of Ca–O intra-layers sandwiched by silicate chains and spaced by interlayer water. Such lattice structures layered along the c-axis leads to strong anisotropy, where the c-axis is commonly more compliant than the in-plane a/b-axis – similar to the presently observed anisotropy in hydromagnesite due to varying degree of edge/corner sharing of Mg–O octahedra.

Compared to lower-density phases common in fast-setting cement systems (ettringite $Ca_6Al_2(SO_4)_3(OH)_{12}{\cdot}26H_2O$ [28], struvite-K $MgKPO_4{\cdot}6H_2O$ [13], and strätlingite $Ca_2Al_2(SiO_2)(OH)_{10}{\cdot}2.5(H_2O)$ [29]), hydromagnesite has about two times the bulk modulus while 25% higher in density, mainly due to the high OH^- and/or H_2O content in the crystal formulation, suggesting less densely packed or connected M–O polyhedral and increased susceptibility to compression. Their $M^{n+}/(OH^- + H_2O)$ atomic ratios of 0.21, 0.17, and 0.32, respectively, in contrast to 0.83 for hydromagnesite. Compared to other magnesium-based cement-related phases, periclase (MgO) is of much higher bulk modulus and density originated from the dense packing of its cubic, Rock-Salt crystal structure, while the sheet-structured brucite ($Mg(OH)_2$) is similar in density but of ~10% lower bulk modulus than hydromagnesite due to the lack of corner/edge sharing between neighboring Mg–O sheets. Compared to anhydrous calcium carbonates (calcite [22] and aragonite [26]), hydromagnesite possesses slightly lower bulk modulus and density by 20% due to the presence of OH^- and H_2O decreasing the packing density and connectivity of Mg–O polyhedra. Besides, hydromagnesite has very similar bulk modulus with calcium aluminate hydrates, and its density falls between CAH_{10} and C_3AH_6., both of which comprises of three-dimensional network of CaO_8 and AlO_6 polyhedra, as MgO_6 polyhedra do in the present hydromagnesite.

4. Conclusions

The present HP-XRD work examines the intrinsic mechanical properties of the crystal lattice of hydromagnesite, a primary binding phase in reactive MgO cement. The critical findings are as follows:

(i) The hydromagnesite sample was hydrostatically pressurized to maximumly 7.7 GPa using a diamond anvil cell and unloaded back to ambient conditions, showing no observable permanent lattice deformation.

(ii) The **a**, **b**, and **c**-axial incompressibility of hydromagnesite are –1/335, –1/171, and –1/219 GPa^{-1}, respectively, up to 7.7 GPa, while the monoclinic angle β remains close (< 0.3°) to its ambient value, all lattice parameters exhibiting full recovery upon complete unloading.

(iii) The bulk modulus of hydromagnesite was determined to be 58.7 ± 1.6 GPa using 2nd-order BM-EoS or 71.2 ± 1.6 GPa using 3rd-order BM-EoS in the hydrostatic pressure range of 0-7.7 GPa.

(iv) Hydromagnesite possesses comparable bulk modulus-density relation as C-(A-)S-Hs, primary Portland cement system binding phases and lies within the bulk modulus-density range of various binding phases from multiple cement systems.

Hydromagnesite is a common binding phase in reactive MgO cement. Understanding of the intrinsic mechanical properties of hydromagnesite from the present study provides essential guidance for engineering green alternatives to conventional Portland cement systems. The present knowledge are valuable for model tuning at the first-principle and atomistic levels and for application in the continuum/bulk-scale simulation and calculations – facilitating the bottom-up materials design methodology.

Acknowledgements

This work was performed under the auspices of the U.S. Department of Energy by Lawrence Livermore National Laboratory (contract No. DE-AC52-07NA27344). Beamline 12.2.2 and the sample preparation of this research were partially supported by COMPRES, the Consortium for Materials Properties Research in Earth Sciences under NSF Cooperative Agreement EAR 1606856. The work was supported by the Department of Energy funded Energy Earthshot Research Center—Center for Coupled Chemo-Mechanics of Cementitious Composites for EGS (C4M).

References

[1] "Technology Roadmap - Low-Carbon Transition in the Cement Industry," International Energy Agency, 2018.

[2] P. S. Fennell, S. J. Davis, and A. Mohammed, "Decarbonizing cement production," *Joule*, vol. 5, no. 6, pp. 1305–1311, Jun. 2021.

[3] G. Habert *et al.*, "Environmental impacts and decarbonization strategies in the cement and concrete industries," *Nat Rev Earth Environ*, vol. 1, no. 11, Art. no. 11, Nov. 2020.

[4] S. A. Miller and R. J. Myers, "Environmental Impacts of Alternative Cement Binders," *Environ. Sci. Technol.*, vol. 54, no. 2, pp. 677–686, Jan. 2020.

[5] S. A. Miller, G. Habert, R. J. Myers, and J. T. Harvey, "Achieving net zero greenhouse gas emissions in the cement industry via value chain mitigation strategies," *One Earth*, vol. 4, no. 10, pp. 1398–1411, Oct. 2021.

[6] C. W. Hargis, I. A. Chen, M. Devenney, M. J. Fernandez, R. J. Gilliam, and R. P. Thatcher, "Calcium Carbonate Cement: A Carbon Capture, Utilization, and Storage (CCUS) Technique," *Materials*, vol. 14, no. 11, Art. no. 11, Jan. 2021.

[7] S. Ruan and C. Unluer, "Influence of mix design on the carbonation, mechanical properties and microstructure of reactive MgO cement-based concrete," *Cement and Concrete Composites*, vol. 80, pp. 104–114, Jul. 2017.

[8] S. Ruan and C. Unluer, "Comparative life cycle assessment of reactive MgO and Portland cement production," *Journal of Cleaner Production*, vol. 137, pp. 258–273, Nov. 2016.

[9] L. Wang, L. Chen, J. L. Provis, D. C. W. Tsang, and C. S. Poon, "Accelerated carbonation of reactive MgO and Portland cement blends under flowing CO2 gas," *Cement and Concrete Composites*, vol. 106, p. 103489, Feb. 2020.

[10] R. Hay and K. Celik, "Hydration, carbonation, strength development and corrosion resistance of reactive MgO cement-based composites," *Cement and Concrete Research*, vol. 128, p. 105941, Feb. 2020.

[11] R. Hay, N. T. Dung, A. Lesimple, C. Unluer, and K. Celik, "Mechanical and microstructural changes in reactive magnesium oxide cement-based concrete mixes subjected to high temperatures," *Cement and Concrete Composites*, vol. 118, p. 103955, Apr. 2021.

[12] S. Ruan, E.-H. Yang, and C. Unluer, "Production of reactive magnesia from desalination reject brine and its use as a binder," *Journal of CO2 Utilization*, vol. 44, p. 101383, Feb. 2021, doi: 10.1016/j.jcou.2020.101383.

[13] J. Li, W. Zhang, and P. J. M. Monteiro, “Mechanical properties of struvite-K: A high-pressure X-ray diffraction study,” *Cement and Concrete Research*, vol. 136, p. 106171, Oct. 2020.
[14] J. Li and W. Zhang, “Preferred orientation of calcium silicate hydrate and its implication to concrete creep,” *Composites Part B: Engineering*, vol. 247, p. 110297, Dec. 2022, doi: 10.1016/j.compositesb.2022.110297.
[15] M. Akao, F. Marumo, and S. Iwai, “The crystal structure of hydromagnesite,” *Acta Cryst B*, vol. 30, no. 11, Art. no. 11, Nov. 1974.
[16] C. Prescher and V. B. Prakapenka, “DIOPTAS: a program for reduction of two-dimensional X-ray diffraction data and data exploration,” *High Pressure Research*, vol. 35, no. 3, pp. 223–230, Jul. 2015.
[17] R. W. Cheary and A. A. Coelho, “CCP14 Homepage - Tutorials and Examples - Peak Fitting using Xfit-Koalariet (Coelho and Cheary) for Win95/NT.” http://ccp14.cryst.bbk.ac.uk/tutorial/xfit-95/xfit.htm (accessed Jul. 31, 2023).
[18] J. Laugier and B. Bochu, “CELREF Version 3 Cell Parameter Refinement Program From Powder Diffraction Diagram.” Laboratoire des Matériaux et du Génie Physique, Ecole Nationale Supérieure de Physique de Grenoble (INPG), France, 2002.
[19] J. Moon, J. E. Oh, M. Balonis, F. P. Glasser, S. M. Clark, and P. J. M. Monteiro, “High pressure study of low compressibility tetracalcium aluminum carbonate hydrates 3CaO·Al2O3·CaCO3·11H2O,” *Cement and Concrete Research*, vol. 42, no. 1, pp. 105–110, Jan. 2012.
[20] J. Li, W. Zhang, K. Garbev, G. Beuchle, and P. J. M. Monteiro, “Influences of cross-linking and Al incorporation on the intrinsic mechanical properties of tobermorite,” *Cement and Concrete Research*, vol. 136, p. 106170, Oct. 2020.
[21] J. Li *et al.*, “The nanomechanical properties of non-crosslinked calcium aluminosilicate hydrate: The influences of tetrahedral Al and curing age,” *Cement and Concrete Research*, vol. 159, p. 106900, Sep. 2022.
[22] S. A. T. Redfern and R. J. Angel, “High-pressure behaviour and equation of state of calcite, CaCO3,” *Contrib Mineral Petrol*, vol. 134, no. 1, pp. 102–106, Jan. 1999.
[23] Fei, Y., 1999. Effects of temperature and composition on the bulk modulus of (Mg,Fe)O. American Mineralogist 84, 272–276. https://doi.org/10.2138/am-1999-0308
[24] J. Li, W. Zhang, and P. J. M. Monteiro, “Structure and Intrinsic Mechanical Properties of Nanocrystalline Calcium Silicate Hydrate,” *ACS Sustainable Chem. Eng.*, vol. 8, no. 33, pp. 12453–12461, Aug. 2020.
[25] G. Geng *et al.*, “A high-pressure X-ray diffraction study of the crystalline phases in calcium aluminate cement paste,” *Cement and Concrete Research*, vol. 108, pp. 38–45, Jun. 2018.
[26] Martinez, I., Zhang, J., Reeder, R.J., 1996. In situ X-ray diffraction of aragonite and dolomite at high pressure and high temperature: Evidence for dolomite breakdown to aragonite and magnesit. American Mineralogist 81, 611–624. https://doi.org/10.2138/am-1996-5-608
[27] Catti, M., Ferraris, G., Hull, S., Pavese, A., 1995. Static compression and H disorder in brucite, Mg(OH)2, to 11 GPa: a powder neutron diffraction study. Phys Chem Minerals 22, 200–206. https://doi.org/10.1007/BF00202300
[28] S. M. Clark, B. Colas, M. Kunz, S. Speziale, and P. J. M. Monteiro, “Effect of pressure on the crystal structure of ettringite,” *Cement and Concrete Research*, vol. 38, no. 1, pp. 19–26, Jan. 2008.
[29] J. Moon, J. E. Oh, M. Balonis, F. P. Glasser, S. M. Clark, and P. J. M. Monteiro, “Pressure induced reactions amongst calcium aluminate hydrate phases,” *Cement and Concrete Research*, vol. 41, no. 6, pp. 571–578, Jun. 2011.
[30] Brandstetter, S., Derlet, P.M., Van Petegem, S., Van Swygenhoven, H., 2008. Williamson–Hall anisotropy in nanocrystalline metals: X-ray diffraction experiments and atomistic simulations. Acta Materialia 56, 165–176. https://doi.org/10.1016/j.actamat.2007.09.007
[31] Himabindu, B., Latha Devi, N.S.M.P., Rajini Kanth, B., 2021. Microstructural parameters from X-ray peak profile analysis by Williamson-Hall models; A review. Materials Today: Proceedings, FRESM’21 47, 4891–4896. https://doi.org/10.1016/j.matpr.2021.06.256
[32] Piermarini, G.J., Block, S., Barnett, J.D., Forman, R.A., 1975. Calibration of the pressure dependence of the R 1 ruby fluorescence line to 195 kbar. Journal of Applied Physics 46, 2774–2780. https://doi.org/10.1063/1.321957